Air Flow and Particle Trajectories around Aircraft Fuselages. Part III: Extensions to Particles of Arbitrary Shape

W. D. KING*

National Center for Atmospheric Research,† Boulder, CO 80307

(Manuscript received 9 November 1984, in final form 8 April 1985)

ABSTRACT

Earlier work that produced generalized rules for obtaining trajectories of water droplets moving around aircraft fuselages has been extended to cover the case for particles of arbitrary shape. The parameters determining the major features of the trajectories are the fuselage radius and a generalized Stokes number that can be used to calculate an equivalent water drop size for particles of arbitrary shape and density. As for water drops, the maximum width of the shadow zone for sampling the particles is about one-fifth of the fuselage radius, and it occurs for those ice columns and plates of typical densities whose major dimensions are about 600 μm and 2 mm, respectively.

1. Introduction

In Part I of this series of papers (King, 1984), it was shown that the airflow around aircraft fuselages could be modeled with sufficient accuracy using distributed sink–source techniques, and that the flow in most regions of interest could be characterized in terms of a scale length equal to the fuselage radius. Examination of water drop trajectories around aircraft fuselages of several different shapes showed that some of the more important features, such as concentration enhancement factors and the width of the particle shadow zone, could be expressed in terms of the same length scale and a dimensionless parameter similar to the Stokes number. At a fuselage location three fuselage radii from the nose, the maximum width of the shadow zone was found to be about 0.2 of a fuselage radius, and it occurred for that combination of drop size, aircraft velocity, etc., for which the Stokes parameter had a value near six. For typical aircraft dimensions and operating conditions this value occurs for droplet diameters in the range 150–200 μm.

Although the nondimensional description of the treatment allowed for extrapolation to drops other than water, its usefulness was nevertheless restricted to particles of spherical shape. Thus, users of ice crystal data obtained by aircraft sampling would find the guidelines of little use. Because so much of the information on the early stages of precipitation development has been obtained through aircraft sampling of ice crystals that occur in a wide variety of shapes, there is considerable interest in extending the rules developed in Part I to cover more general shapes. The only work performed in this area is that of Norment and Zalosh (1974) and Norment (1975), who provided detailed information such as enhancement factors for various ice crystal shapes moving around three different aircraft, but they did not attempt to generalize their results in any way.

In this paper the work of Part I is extended to cover particles of more general shape. In most cases the emphasis will be on ice crystal plates and columns, but the results are readily applicable to other solid shapes moving through air. As in Part I, the results are restricted to fuselages at zero angle of attack in steady potential flow. Extensions to finite angles of attack and flows with large-scale turbulence will form the basis of future work.

2. General background

a. Equation of motion

The vector equation used to describe the motion of a body of arbitrary shape was taken as

$$m d\mathbf{U}/dt = \frac{1}{2} C_d \rho_a A |\mathbf{Q} - \mathbf{U}|^2 (\widehat{\mathbf{Q} - \mathbf{U}}) + m\mathbf{g}, \quad (1)$$

where m is the mass of the particle, $\mathbf{Q}$ and $\mathbf{U}$ are the air and particle velocity vectors, respectively, (and the cap denotes a unit vector), C_d is the steady-state drag coefficient, A the cross-sectional area of the particle when projected on a plane at right angles to the relative flow vector $\mathbf{Q} - \mathbf{U}$, ρ_a the density of air, and $\mathbf{g}$ is gravitational acceleration. The local Reynolds number Re along the trajectory is given by

$$\mathrm{Re} = \rho_a |\mathbf{Q} - \mathbf{U}| d/\eta, \quad (2)$$

* Permanent affiliation: Cloud Physics Laboratory, CSIRO Division of Atmospheric Research, Sydney, Australia.

† The National Center for Atmospheric Research is sponsored by the National Science Foundation.

where d is the characteristic length scale of the particle and η the viscosity of the air. Using (2) and normalizing (1) to a velocity scale equal to the free stream velocity V, a length scale b, and a time scale $\tau = tV/b$, we have

$$d\mathbf{u}/d\tau = \frac{C_d R_e}{24S}(\mathbf{q} - \mathbf{u}) + F\hat{\mathbf{g}}. \tag{3}$$

In (3), $\mathbf{u} = \mathbf{U}/V$, $\mathbf{q} = \mathbf{Q}/V$, F is the Froude number:

$$F = gb/V^2; \tag{4}$$

S is a generalization of the Stokes number defined in Part I, and for a particle of arbitrary shape it is given by

$$S = mdV/12A\eta b. \tag{5}$$

Given the results shown in Part I, it is logical to take the length scale b as equal to the fuselage radius. Note that for the case of a sphere of density ρ_p, $S = d^2\rho_p V/18\eta b$, as in Part I.

Determination of particle trajectories is obtained by integration of (3) forward in time, subject to three assumptions, which will be discussed in turn. These are: i) the drag coefficients for steady motion can be used even though the particle is being accelerated; ii) the particle has a sufficiently fast rotational response time to be able to present its maximum cross-sectional area to the relative-flow vector $\mathbf{Q} - \mathbf{U}$ at all times; iii) the particles do not tumble or gyrate.

b. *Drag for accelerated motions*

At present there is no formal description for the force on an accelerating body of arbitrary shape undergoing general three-dimensional motion at high Re. We will proceed to develop an order-of-magnitude relation for ellipsoids of revolution that can provide useful approximation to disks and columns. In the following, we adopt the usual approach of approximating a plate of thickness-to-diameter ratio k as an oblate ellipsoid of the same axis ratio, and a column of length-to-diameter ratio k as a prolate ellipsoid of the same axis ratio.

The motion of a sphere in accelerated rectilinear motion starting from rest is described by Clift *et al.* (1978, p. 296):

$$\dot{u} = C_d\,\mathrm{Re}(q - u)/24S + \rho_a V_p \dot{u}/2m + 1.5d^2(\pi\rho_a\eta b/m^2V)^{1/2}\int_0^\tau \dot{u}(\tau')(\tau - \tau')^{-1/2}d\tau', \tag{6}$$

where the over-dot signifies differentiation with respect to time, and V_p is the particle volume. This equation, which is a special case of the one proposed by Odar and Hamilton (1964), was based on an empirical extension of a similar one theoretically derived for creeping flow (i.e., Re < 1). The two "extra" terms on the right-hand side of (6) account, respectively, for the added inertia of the surrounding air and a "history" term associated with the diffusion of vorticity away from the sphere. (See Morton, 1984, for a good description of how vorticity is generated by an accelerating surface.) For the sphere, it has been shown that the form of these acceleration-dependent terms is identical for both creeping flow and high Re flow, and we can argue in a nonrigorous fashion that we might expect the same to be true for ellipsoids. Under this assumption, the acceleration-dependent inertia and history force terms would be multiplied by geometry-related functions $f(k)$ and $g(k)$, respectively, where k is the axis ratio for the ellipsoid (i.e., $k < 1$ for oblate spheroids, $k > 1$ for prolate spheroids) and $f(k)$ and $g(k)$ are given by (Clift *et al.*, 1978, p. 292):

$$f(k) = \begin{cases} 2[k\cos^{-1}k - (1 - k^2)^{1/2}] \\ \quad \times [k^2(1 - k^2)^{1/2} - k\cos^{-1}k]^{-1}, & \text{(oblate)} \\ -2 + 8(k^2 - 1)^{3/2}\{4(k^2 - 1)^{3/2} \\ \quad - 2k^2(k^2 - 1)^{1/2} + k\ln[k + (k^2 - 1)^{1/2}]/ \\ \quad [k - (k^2 - 1)^{1/2}]\}^{-1}, & \text{(prolate),} \end{cases} \tag{7}$$

$$g(k) = \begin{cases} (4 + k)^2/25, & \text{(oblate)} \\ (3 + 2k)^2/25, & \text{(prolate).} \end{cases} \tag{8}$$

In (8), $f(k)$ and $g(k)$ have been evaluated for motion of the ellipsoid parallel to the symmetry axis for the oblate case, and lateral to the symmetry axis for the prolate case; i.e., we have only defined $f(k)$ and $g(k)$ for those motions for which the maximum cross-sectional area is across the flow. Allowing for the multiplier $f(k)$, examination of (6) shows that the ratio of the fluid inertia term to the usual steady state drag term is given by $f(k)\rho_a/2\rho_p$, where ρ_p is the particle density. Evaluation of (7) for the prolate case shows that $f(k)$ has a maximum value of two, so that neglecting the fluid inertia term in calculating the drag of columns would cause a maximum relative error of ρ_a/ρ_p, which is typically of the order of 10^{-2} to 10^{-3} for sampling particles in air. For an oblate spheroid, however, $f(k) \approx 4/\pi k$ for small k, so that $f(k) \to \infty$ as $k \to 0$. Physically this occurs because the volume of fluid interacting with the disk remains finite even as the thickness and mass of the disk become very small. For cloud physics applications, where the thickness-to-diameter ratio of plates would typically be of the order of 10^{-1} but possibly as small as 10^{-2} for particles greater than 1 mm diameter (Pruppacher and Klett, 1980), the errors in neglecting the fluid inertia term in calculating the drag on plates could therefore be as high as 5%.

To examine the contribution of the history term to the total drag, we note that for motions in which $\dot{u}(\tau')$ is increasing with time (which is generally the case for particles moving around the nose region of the fuselage) an upper limit for the integral can be found, because $\dot{u}(\tau') < \dot{u}(\tau)$ for $\tau' < \tau$, and can thus be taken outside

the integral. Then the ratio of the history-drag to the steady-state drag can be shown to be less than

$$(3\rho_a/\rho_p)(\pi\nu_a t)^{1/2}[g(k)d^2/V_p],$$

where ν_a is the kinematic viscosity of the air. When simplified further using (8), this expression is equal to the product of two ratios: one is the ratio of fluid to particle densities, while the second is the ratio of the length scale for vorticity diffusion ($\sqrt{\nu t}$) to a particular dimension of the particle [$V_p/g(k)d^2$]. For prolate bodies (i.e., columns) it turns out that this length scale is the length, while for oblate bodies (i.e., plates), it is the thickness dimension, c. Therefore again the added drag is maximized for very thin plates. Taking $t \approx 10^{-1}$ s (this is a conservative assumption, since it is equivalent to allowing the acceleration to take place over a distance of five fuselage radii), the relative effect is still only 5% for a 40-μm-thick plate.

The use of steady-state drag coefficients is therefore unlikely to cause any major errors in computing the trajectories of columns, but the very conservative treatment outlined above suggests that for large thin plates the steady-state drag coefficients used could possibly be low by as much as 10%. Bearing in mind that the drag coefficient enters the calculations as C_d Re/24S, another way of interpreting this is that we may have computed the trajectory for a particle whose Stokes parameter is actually 10% higher than it is thought to be. Thus the trajectory computed for a 500-μm-diameter plate could possibly be that for a 530-μm-diameter plate. In the context of this treatment, which is aimed at producing rules of thumb, and in the context of our present measurement abilities with respect to ice crystals, such uncertainties are of little consequence.

c. *Orientation of particles with respect to the flow*

When freely falling under gravity in the atmosphere, particles such as columns and plates usually fall with their maximum cross-sectional area across the flow direction, and, indeed, information on drag characteristics is usually available for this orientation only. In calculating the motions of particles around aircraft fuselages we are concerned with situations in which the relative flow vector can change direction at a rate of the order of tens of degrees per second. It is therefore important to know whether the crystals can rotate fast enough to keep up with this changing direction—determination of their trajectories obviously becomes a very complex problem if we have to contend with a rotational equation of motion as well as a translational one. Norment and Zalosh (1974) chose to examine this aspect of the problem by calculating trajectories for columns aligned across or along the direction of relative flow for the entire trajectory. The differences obtained were substantial, so it is of some interest to examine the problem in more detail. To do so, we require information on two rate processes: (i) the rate of change of orientation of an ice crystal in response to the aerodynamic forces on it and (ii) the rate of change of angle of the relative flow.

For the first aspect we need to be able to compute the torque on a crystal at an angle θ to the relative flow, as seen in Fig. 1. Estimation of this torque is comparatively easy for two ranges of Reynolds number, $\leqslant 1$ and $\geqslant 10^3$. For the low Re range (Stokes flow), it can be shown (Happel and Brenner, 1965) that for bodies with sufficient symmetry, such as columns, plates, etc., there is no torque on the body at all. In the high Re regime the torque can be reasonably approximated by taking half the torque calculated using potential flow theory. This can be done because the pressure distribution on the front of the body is close to the potential flow one, and flow separation generally removes the torque contribution supplied by the pressure distribution on the rear half of the body.

In Fig. 2 we have plotted the Reynolds number along the trajectories of a column and a plate moving at 90 m s^{-1} around the top of a Fokker F-27 aircraft fuselage. The Stokes parameter for both particles was five. It is apparent that the local Re falls in the regime where it is most difficult to compute the torque. (The nonzero Re several aircraft diameters ahead of the nose is due to gravitational settling.) However, in the region near the aircraft nose (i.e., $-1 < x < 1$), the Reynolds number is always >30, and $\sim 10^2$ near the cockpit. For this Reynolds number regime the work of Le Clair *et al.* (1970) would suggest that the pressure distribution is more akin to the potential flow one than the Stokes flow one. To be conservative, we shall assume the torque is only one-tenth of that calculated from potential flow theory. For slender bodies at small angles of attack the potential flow torque is given by

$$T = \frac{1}{2}\rho_a|\mathbf{Q} - \mathbf{U}|^2 \sin 2\theta V_p. \tag{9}$$

For more blunt ellipsoids this expression needs to be multiplied by a shape factor $h(k)$ that is similar to the functions $f(k)$ and $g(k)$ given earlier. In fact, for k

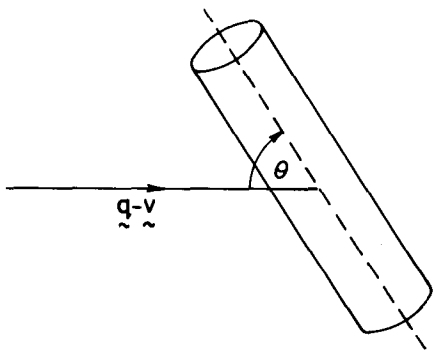

FIG. 1. Geometry of orientation angle of crystal.

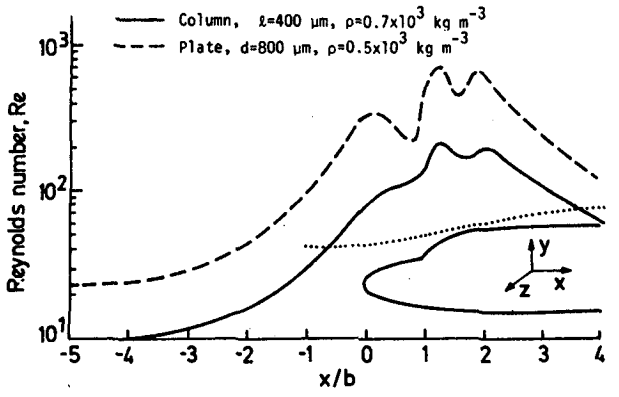

FIG. 2. Local Reynolds number along the trajectory shown (dotted line) for two particles whose Stokes parameter is 5.

≥ 3, Weinheimer's (1980) results show $h(k) = f(k)/2$ to within 15% for both prolate and oblate ellipsoids. Thus we will take the torque on the crystal to be

$$T = \rho_a|\mathbf{Q} - \mathbf{U}|^2 f(k) \sin 2\theta V_p/40. \quad (10)$$

Therefore, the rotational equation of motion for the ice crystal near the fuselage would be

$$I\ddot{\theta} + T = 0, \quad (11)$$

where I is the moment of inertia about the appropriate axis ($ml^2/12$ for columns, $3md^2/64$ for plates). In (11) we have ignored any torque that opposes the motion of the crystal once it begins to rotate. We can do this *a posteriori* because the rotational velocities (i.e., $l\dot{\theta}$ or $d\dot{\theta}$) are much smaller than the relative flow velocity $|\mathbf{Q} - \mathbf{U}|$ by virtue of the small dimensions of the ice crystals. Making the usual small-angle approximation allows us to solve (11) as a harmonic oscillator with characteristic frequency:

$$\left.\begin{aligned} \omega_c &= 1.1(\rho_a/\rho_p)^{1/2}\, \mathrm{Re}\nu a/(ld) \quad \text{for columns} \\ \omega_p &= 1.1(\rho_a/\rho_p)^{1/2}\, \mathrm{Re}\nu a/(d^3 c)^{1/2} \quad \text{for plates} \end{aligned}\right\}. \quad (12)$$

In (12) we have expressed the velocity difference $|\mathbf{Q} - \mathbf{U}|$ in terms of the Reynolds number along the trajectory.

We now turn to examine the rate at which the direction of the drag vector is changing. This direction can be specified in terms of the angles α and β that the relative flow vector makes with the x and y axes when projected on to the x–z and y–z planes, respectively. Thus $\alpha = \tan^{-1}(q_y - u_y)/(q_x - u_x)$ and $\beta = \tan^{-1}(q_z - u_z)/(q_x - u_x)$, and we are interested in $\dot{\alpha}$ and $\dot{\beta}$ along the particle trajectory. In Fig. 3 we have plotted $\dot{\alpha}$ and ω_c for the column trajectory as shown in Fig. 2 ($\dot{\beta} = 0$ by virtue of the symmetry in this case and in general is $<\dot{\alpha}$ because shape-changes around the sides of aircraft are generally smoother than those on the top). Although we see that $\dot{\alpha}$ can be as high as 200 rad s^{-1}, in general it is less than one-tenth of ω_c. The crystals are therefore moving in a situation where the equilibrium angle changes at a rate that is less than one-tenth the rate at which the crystal can rotate. It is therefore highly unlikely that the crystal will be at an orientation far removed from the equilibrium angle. Two points here are worthy of comment: i) the high values of $\dot{\alpha}$ and ω_c are due to the fact that the particles pass through the critical regions in a time of the order of 10^{-2} s; ii) $\dot{\alpha}$, $\dot{\beta}$ do not describe the rates of change of the angles of the air streamlines [these would be given by the time differential of $\tan^{-1}(q_y/q_x)$, etc.]. They are rates of change of angles that themselves are given in terms of ratios of two velocity differences—this in part explains the nonmonotonic nature of the curve for $\dot{\alpha}$ in Fig. 3, since $(q_y - u_y)$ and $(q_x - u_x)$ are by no means in phase.

The same inequality between $\dot{\alpha}$ and ω_c, ω_p can be shown to hold for a wide variety of column and plate sizes. Even though the above treatment is not valid at distances further than about one fuselage radius ahead of the nose (because in this region the Reynolds number is less than 30, and we begin to lose confidence in our estimate of the aerodynamic torque), calculations show that when the drag coefficient is artificially reduced by an order of magnitude for the region from $x/s = \infty$ to -1 (to gauge the effect of the possibility of columns or plates being end-on to the flow here) the difference in the position of the shadow zone is less than 0.2% of a fuselage radius.

Thus we are led to the conclusion that in those regions that largely determine the particle trajectory the crystal rotational response time is sufficiently small to

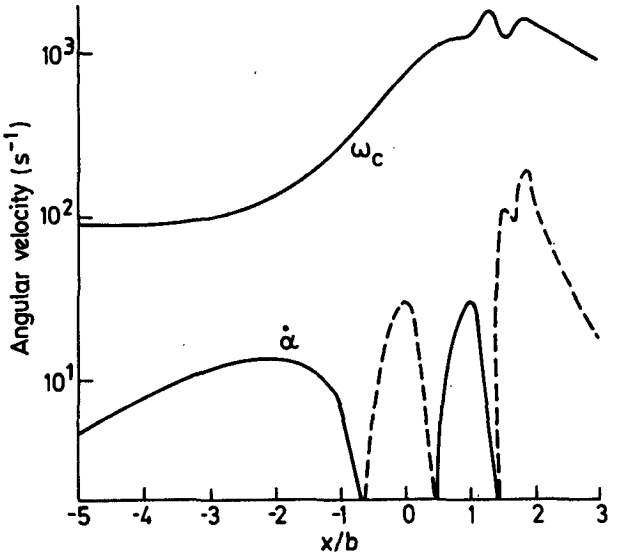

FIG. 3. A comparison between the aerodynamic angular velocity of a column along a trajectory (ω_c) and the rate at which the drag vector is changing direction ($\dot{\alpha}$). The dashed section of the curve for $\dot{\alpha}$ is negative.

allow it to respond to changes in direction of the drag vector, and the assumption that its maximum cross-sectional area will be across the relative flow is an appropriate one to make.

d. Tumbling

In Section 2c we examined the problem of whether crystals could rotate fast enough; in this section we look at the other extreme of rotational dynamics—i.e., whether there is any possibility that the crystals could be in a continuously rotating or tumbling mode.

The most extensive experimental work in this area was performed by Stringham *et al.* (1969), who observed the fall behavior of various shapes under laboratory conditions. In general, they found the fall patterns could be classified according to the Re regime. For cylinders with $400 < \mathrm{Re} < 8000$, there were oscillations about the equilibrium position of the type described in Section 2c, the amplitude of the oscillations increasing with Re. For $\mathrm{Re} > 8000$ there were additional oscillations in the horizontal plane about a vertical axis, and the fall pattern became unstable.

For disks the stable region occurred for $10 < \mathrm{Re} < 120$. For $120 < \mathrm{Re} < 2000$, there was a gradual transition from stable fall behavior to increasing oscillatory motions until the tumbling was fully developed at the top end of this range.

For a given size particle the maximum Re occurs at impaction or near impaction for a glancing trajectory of the type shown in Fig. 2. For columns and plates whose maximum dimension was 1 mm, the maximum Re along a glancing trajectory was 600 and 800, respectively. On the basis of the Stringham *et al.* (1969) results, it is therefore unlikely that plates or columns would tumble during their passage around aircraft fuselages at typical sampling speeds.

From this and the findings of the previous section, we conclude that ice crystals will present a particular orientation to a sampling device dependent on its location with respect to the airflow distortions. The variation of this orientation with sampling position is a separate topic in itself and will be the subject of a future publication.

3. Particle trajectories

Having established the validity of using (3) with steady-state drag coefficients as the equation of motion for ice crystals moving past aircraft fuselages, we now present results obtained by integrating this equation forward in time from a point 20 fuselage radii ahead of the nose, where it was assumed that conditions were equal to those of the free stream. A fourth-order Adams-Bashforth scheme was used for the integration, and the drag coefficients for spheres and columns taken from Norment and Zalosh (1974), while the Reynolds number/Best number relationships of Pruppacher and Klett (1980) were inverted for use with plates. The Auer and Veal (1970) thickness-diameter relationship was used for the plates, and the columns were taken to have a diameter-to-length ratio of 0.5.

a. Depletion zone

The depletion or shadow zone is that region in which particles of a given size cannot be sampled because there are no particle trajectories through the region (see Fig. 2 or Fig. 6 of Part I). In Fig. 4 the nondimensional width of the shadow zone for a position at $x/b = 3$ on top of an F-27 aircraft is shown as a function of Stokes parameter for water drops, columns of two different densities, and plates. When presented in this form there is very little in common between the curves, except that the maximum depletion zone width is about 0.15 for all particle shapes. From Part I we know that S is the dominating parameter in determining the trajectories of particles of a given shape, but for this to remain true for a variety of shapes two conditions must be fulfilled. First, the curve relating C_d to Re should be similar for all particle shapes. That this is true can be seen from Fig. 5. For a given Re, variations in C_d for three different shapes of interest are less than 40%. This variation is small when compared with the three or four order-of-magnitude changes in S of interest to cloud physicists. Also, variations in Re along a trajectory in the critical areas should be sufficiently small that the concept of an average C_d Re is realistic, and there should be little differences between the average Reynolds numbers from one particle shape to another. Reference to Fig. 2 shows that the first part of this condition holds (helped by the fact that the variation of C_d with Re is not significantly different from Re^{-1}). However, it is also apparent that the average Re for the plate trajectory is significantly higher than that of

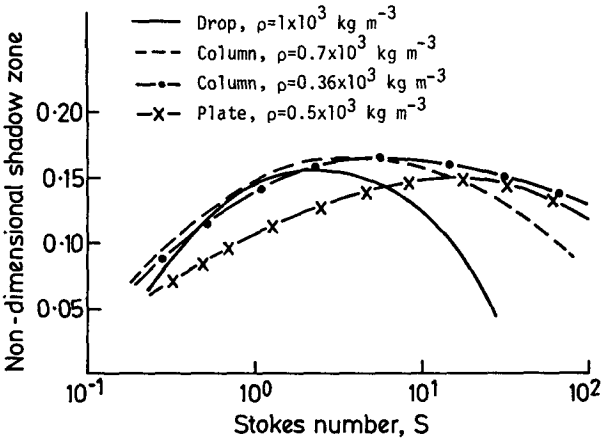

FIG. 4. Variation of shadow zone width as a function of Stokes parameter for various particle shapes.

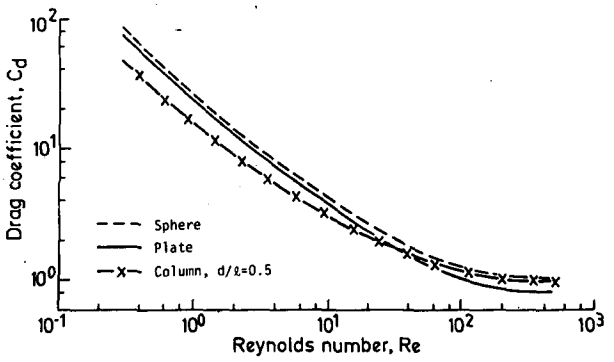

FIG. 5. Drag coefficients for spheres, plates and columns.

the companion column trajectory. This follows directly from the definition of S and Re: for a column and a plate of equal S value on a dimensionally similar trajectory, the diameter of the plate is necessarily greater than that of the column (because of the definition of S), with the consequence that the Reynolds number is correspondingly larger as well.

We might therefore expect to improve the agreement between the curves of Fig. 4 by dividing the S values by the average ratio of the actual drag to the Stokes drag for the particle in question. For columns of density 0.7×10^3 kg m^{-3} the ratio is 7, for columns of density 0.36×10^3 kg m^{-3} it is 8, but for plates of density 0.5×10^3 kg m^{-3} the ratio is about 20. If we define these empirically determined drag factors as f, then the results of a renormalization of S as S/f on the data of Fig. 4 can be shown as in Fig. 6. The improvement, at least for $S \leqslant 6$, is sufficiently large to justify the technique, and the f factors are sufficiently uniform for a wide range of S values to be of practical use.

The disparity in the curves for $S \geqslant 6$ occurs because large particles of identical S values but different shapes have widely different terminal velocities. [The effects of gravity only really become significant for large S values; see Eq. (3).] For many applications these differences are not of great concern, because they occur for particles that are greater in size than those for which the flow distortion effects are maximized. Assuming instruments are sited so that the desired sampling accuracy is achieved for particles of $S \approx 6$, particles larger than this will automatically also be sampled to at least similar accuracies.

It is of some interest to note that the main features of Fig. 6, i.e., the general shape and maximum at 0.15, can be obtained analytically on the basis of a few simple assumptions. This is done in section 3c.

b. *Enhancement factors*

All of the calculations performed in this paper are for conditions identical to those in Part I; i.e., $V = 90$ m s^{-1}, density of air = 1.055 kg m^{-3}, and $\eta = 1.74 \times 10^{-5}$ kg m^{-1} s^{-1}. These are appropriate to sampling at an altitude of about 2 km. For sampling at much higher altitudes (e.g., 6 km) the Reynolds numbers are less than presented here by as much as 50%. The differences in details of trajectories, etc., due to particle shapes as reported in this paper are consequently likely to be the maximum encountered.

Concentration enhancement factors have been calculated in the same manner as in Part I for water drops, ice columns, and plates moving over the upper surface of the F-27 (see Fig. 7). As expected, the four sets of curves of enhancement factors against distance from the skin are similar, again demonstrating the generality of the approach. Differences in the curves are equivalent to an uncertainty of ±0.03 of a fuselage radius.

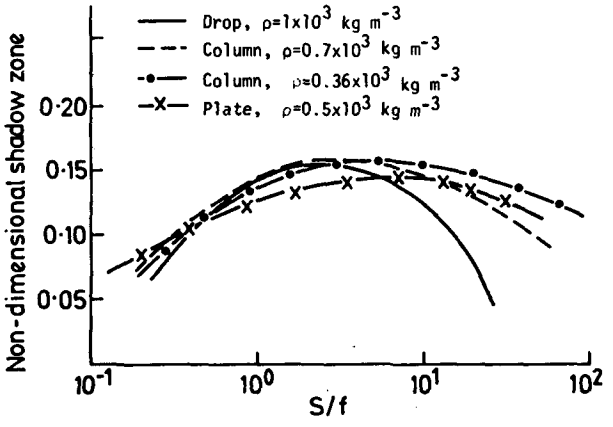

FIG. 6. As for Fig. 4, but with the Stokes parameter renormalized by the average drag for each particle shape.

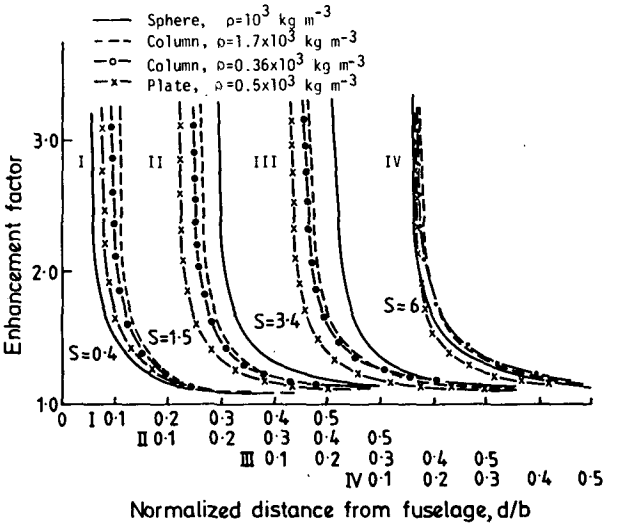

FIG. 7. Enhancement factors for various particle shapes as a function of distance from the fuselage.

This is similar in magnitude to the variations due to different aircraft shapes, as demonstrated in Part I, and for most research aircraft it amounts to an uncertainty of about 6 cm.

The results of Figs. 4, 6, and 7 allow, of course, for an approximate equivalence between particles of different shapes via the definition of the Stokes parameter. Thus a water drop of diameter 50 μm could be expected to behave in a similar fashion to a column of length 170 μm, diameter 85 μm, and density of 0.36×10^3 kg m^{-3}, and many of the general rules of Part I for water drops could be used for ice crystals of different shapes. Some equivalence sizes are listed in Table 1. One feature that is readily apparent from Table 1 is that the equivalent drop diameter of an ice column varies inversely with the density. This arises through the definitions of S and Re, as previously mentioned, and because the drag on columns is largely independent of their length. This result could also have been inferred from a normalization of the data of Norment and Zalosh (1974).

c. *Variation of shadow zone width with distance aft*

All of the foregoing results, as well as those in Part I, pertain to a fuselage station about three fuselage radii back from the nose. As can be seen from Fig. 2, the width of the shadow zone is moved out if the sampling location is further aft. In this section we present a simple analytical model that describes this feature.

Consider first the upper surface. We note that the width of the shadow zone is determined by the glancing trajectory of that particle that just clears the front upper portion of the fuselage (see Fig. 2). The remaining portion of the trajectory is determined by the particle's upward velocity as it clears the cockpit and its subsequent motion in the region behind the cockpit, where the vertical velocity of the air is negligible. In the following model we make two assumptions that allow for this trajectory to be derived analytically. First we assume that the particle has vertical velocity u_t as it enters

TABLE 1. Equivalent water drop diameters for different ice particle shapes.

Water drop diameter (μm)	Ice column diameter for $\rho = 0.7 \times 10^3$ (μm)	Ice column diameter for $\rho = 0.36 \times 10^3$ (μm)	Plate diameter for $\rho = 0.5 \times 10^3$ (μm)
25	29	42	110
50	58	85	288
75	86	126	501
100	115	169	750
125	144	211	1018
150	1173	253	1308
200	231	337	3410

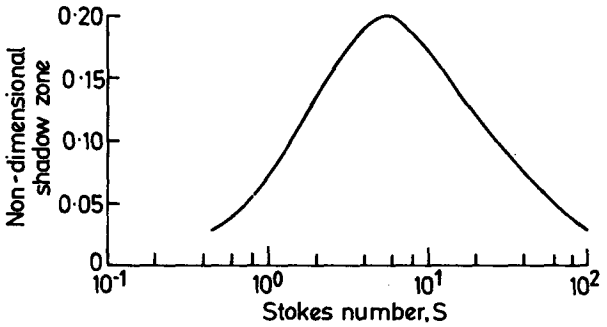

FIG. 8. Predicted variation of shadow zone width with S based on simple analytic model.

a region of the flow field where the upward velocity is q_1 for a time τ_1. For the F-27, $q_1 \approx 0.5$, and $\tau_1 \approx 0.5$ and in more general terms $q_1 = \tan\theta$, where θ is the slope of the critical fuselage section. Then we assume that after receiving a vertical velocity increase from the time spent in this region, the particle clears the edge of the fuselage and enters a region where the external field has unity horizontal velocity and zero vertical velocity. The particle is in this region for a time τ_2 proportional to the distance aft.

The one-dimensional equation describing motion in the vertical is thus for the first region,

$$du_y/d\tau = \alpha(q_1 - u_y) - F, \tag{13}$$

where $u_y(0) = u_t$, $q_1 = 0.5$, and $\alpha = C_d\,\mathrm{Re}/24S$. If we take $C_d\,\mathrm{Re}/24 \approx 7$, as noted in Section 3a, we then have $\alpha = 7/S$. Integration of (13) for a time τ_1 gives

$$u_y(\tau_1) = u_t e^{-\alpha\tau_1} + (q_1 - F/\alpha)(1 - e^{-\alpha\tau_1}), \tag{14}$$

which then becomes the initial velocity for the second region, where the equation of motion is

$$du_y/d\tau = -\alpha u_y - F. \tag{15}$$

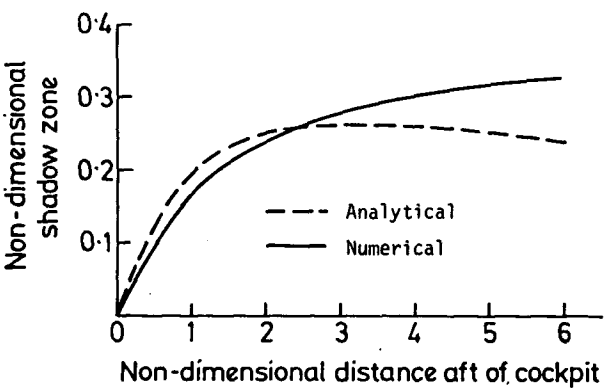

FIG. 9. Variation of shadow zone width with distance aft of the cockpit hump—a comparison between the analytic model and numerical results.

Integration of (15) twice for a time τ_2 yields the width of the shadow zone as

$$y(\tau_2) = \alpha^{-1}\{[(q_1 - F/\alpha)(1 - e^{-\alpha\tau_1}) + u_t e^{-\alpha\tau_1} + F/\alpha](1 - e^{-\alpha\tau_2})\} - F\tau_2/\alpha. \quad (16)$$

This expression is plotted in Fig. 8 as a function of S for $q_1 = 0.5$, $\tau_1 = 1.0$, $\tau_2 = 1.0$, $u_t = -0.01$, $C_d\,\mathrm{Re}/24 = 7$. It is apparent that it explains most of the major details of Fig. 4, i.e., the maximum of about 0.2 at an S value of about 6. Obviously better agreement could be had by adjusting the values of q_1, τ_1, τ_2 etc., but the values chosen are physically sensible and there seems little point in fine-tuning this simple model.

Equation (16) also implies that the width of the shadow zone increases with τ_2 (i.e., distance along the fuselage), a feature quite obvious from inspection of Fig. 1. The predictions of (16) are compared against the full numerical calculations in Fig. 9, and we can see that the agreement is quite reasonable. These data can be used to generalize the results of this paper to other fuselage stations in the manner described in section 3d.

It is expected that a simple model such as this will prove useful in predicting, at least qualitatively, the effects a finite element of attack will have on such features as the width of the shadow zone.

d. Comparison

As an example of the usefulness and generality of results of this paper, we will compare some of the results of Norment and Zalosh (1974) obtained for a Cessna Citation with those predicted from the present paper. In Fig. 10 we have presented Norment and Zalosh's data for the precipitation spectrometer sampling position on the Citation. In terms of the plane of the trajectory the fuselage radius was taken as 77 cm, so that the sampling position was at $d/b = 0.3$ and 1.76 fuselage radii back from the cockpit hump. According to Fig. 9, the shadow zone on the Citation should therefore be 0.06 fuselage radius further out than on the F-27 at one fuselage radius back from the cockpit. We have therefore used our existing F-27 data at $d/b = 0.24$ for the comparison, and this is also shown in Fig. 10. From our point of view, there are two important features of this figure: i) the separate particle-shape curves of Norment and Zalosh are very similar when plotted in terms of S and ii) the values predicted from the F-27 data are extremely close to an average of the Norment and Zalosh data. Given the difference in aircraft dimensions, shape, and sampling locations, this is a powerful result.

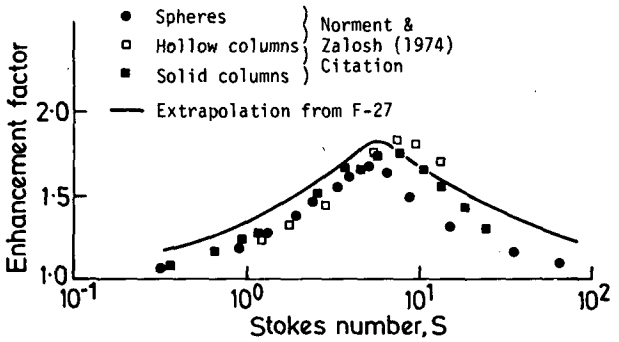

FIG. 10. A comparison between enhancement factors computed by Norment and Zalosh (1974) for a Cessna Citation and those obtained by extrapolating from F-27 results.

4. Conclusions

Previous work has shown that concentration enhancement factors and depletion zones for water drop trajectories around aircraft could be calculated in terms of a normalized fuselage radius and a parameter similar to the Stokes number. This work has now been extended to cover particles of more general shape, although the emphasis has been on ice crystals. Particular conclusions that can be drawn include the following:

a) The usual steady state drag coefficients can be used with little loss of accuracy.

b) Rotational time constants for crystals are sufficiently small to enable them to present their maximum cross-sectional area to the relative flow vector, yet the Reynolds numbers along nonimpacting trajectories are not so high that tumbling would occur.

c) For a typical sampling location about three fuselage radii from the nose, the maximum depletion zone width is about one-fifth of a fuselage radius and occurs when the Stokes number is ~6. Ice crystals whose Stokes numbers are <6 have well-defined equivalent water drop radii, allowing the use of enhancement factors for drops calculated in Part I to be applied immediately to these crystals.

d) The width of the depletion zone increases with distance aft at a rate of about 0.05 of a fuselage radius further out for every fuselage radius further aft.

e) A simple analytical treatment is surprisingly accurate in predicting many features of the depletion zone.

The accuracy of the rules of thumb generated in Part I and now usable on ice crystals should allow researchers to calculate within ±6 cm how far out from the fuselage they should place ice crystal sampling instruments so that they will sample free-stream conditions to within a given accuracy. If more precise calculations are required, then recourse to the full aircraft shape simulation technique and trajectory calculations outlined in Part I can be made.

Acknowledgments. The author wishes to acknowledge useful discussions with Dr. A. Weinheimer and Dr. R. Rasmussen of NCAR. This work was carried out when the author was on leave from CSIRO at NCAR, and it is a pleasure to acknowledge the assistance of Jack Warner, Byron Phillips, and Darrel Baumgardner in facilitating that visit.

REFERENCES

Auer, A. H., and D. L. Veal, 1970: The dimensions of ice crystals in natural clouds. *J. Atmos. Sci.*, **27**, 919–926.

Clift, R., J. R. Grace and M. E. Weber, 1978: *Bubbles, Drops, and Particles.* Academic Press, 389 pp.

Happel, J., and H. Brenner, 1965: *Low Reynolds Number Hydrodynamics.* Prentice-Hall, 553 pp.

King, W. D., 1984: Air flow and particle trajectories around aircraft fuselages. Part I: Theory. *J. Atmos. Oceanic Technol.*, **1**, 5–13.

Le Clair, B. P., A. E. Hamielec and H. R. Pruppacher, 1970: A numerical study of the drag on a sphere at low and intermediate Reynolds numbers. *J. Atmos. Sci.*, **27**, 308–315.

Morton, B. R., 1984: The generation and decay of vorticity. *Geophys. Astrophys. Fluid Dyn.*, **28**, 277–308.

Norment, H. G., 1975: Effects of airplane flowfields on cloud water content measurements. Report AFCRL-TR-75-0231, Air Force Cambridge Research Laboratories, Hanscom AFB, MA, 72 pp.

——, and R. G. Zalosh, 1974: Effects of airplane flowfields on hydrometeor concentration measurements. Report AFCRL-TR-74-0602, Air Force Cambridge Research Laboratories, Hanscom AFB, MA, 101 pp.

Odar, F., and W. S. Hamilton, 1964: Force on a sphere accelerating in a viscous fluid. *J. Fluid Mech.*, **18**, 302–314.

Pruppacher, H. R., and J. D. Klett, 1980: *Microphysics of Clouds and Precipitation.* Reidel, 714 pp.

Stringham, G. E., D. B. Simons and H. P. Guy, 1969: *The Behaviour of Large Particles Falling in Quiescent Liquids.* Geological Survey Prof. Pap. 562-C, U.S. Government Printing Office, Washington, DC, 36 pp.

Weinheimer, A. J., 1980: The rotational dynamics of atmospheric ice: Electrical and aerodynamic torques. Ph.D. thesis, Rice University, 126 pp.